

1 **Last ice sheet recession and landscape emergence above sea level in east-central Sweden, evaluated**  
2 **using *in situ* cosmogenic <sup>14</sup>C from quartz**

3  
4 Bradley W. Goodfellow<sup>1\*</sup>

5 Arjen P. Stroeven<sup>2,3</sup>

6 Nathaniel A. Lifton<sup>4,5</sup>

7 Jakob Heyman<sup>6</sup>

8 Alexander Lewerentz<sup>1</sup>

9 Kristina Hippe<sup>7</sup>

10 Jens-Ove Näslund<sup>8</sup>

11 Marc W. Caffee<sup>4,5</sup>

12

13 <sup>1</sup>Geological Survey of Sweden

14 <sup>2</sup>Department of Physical Geography, Stockholm University

15 <sup>3</sup>Bolin Centre for Climate Research, Stockholm University

16 <sup>4</sup>Department of Earth, Atmospheric, and Planetary Sciences, Purdue University

17 <sup>5</sup>Department of Physics and Astronomy, Purdue University

18 <sup>6</sup>Department of Earth Sciences, University of Gothenburg

19 <sup>7</sup>Umweltplanung Dr. Klimsa

20 <sup>8</sup>Swedish Nuclear Fuel and Waste Management Company (SKB)

21

22 \*Corresponding author: [bradley.goodfellow@sgu.se](mailto:bradley.goodfellow@sgu.se)

23

24 **Abstract**

25 *In situ* cosmogenic <sup>14</sup>C (*in situ* <sup>14</sup>C) in quartz provides a recently developed tool to date exposure of  
26 bedrock surfaces up to ~25,000 years. From outcrops located in east-central Sweden, we test the  
27 accuracy of *in situ* <sup>14</sup>C dating against (i) a relative sea level (RSL) curve constructed from radiocarbon  
28 dating of organic material in isolation basins, and (ii) the timing of local deglaciation constructed from  
29 a clay varve chronology complemented with [traditional](#) radiocarbon dating. Five samples of granitoid  
30 bedrock were taken along an elevation transect extending southwestwards from the Baltic Sea coast  
31 near Forsmark. Because these samples derive from bedrock outcrops positioned below the highest  
32 postglacial shoreline, they target the timing of progressive landscape emergence above sea level. In  
33 contrast, *in situ* <sup>14</sup>C concentrations in an additional five samples taken from granitoid outcrops above  
34 the highest postglacial shoreline, located 100 km west of Forsmark, should reflect local deglaciation

35 ages. The ten *in situ* <sup>14</sup>C measurements provide robust age constraints that, within uncertainties,  
36 compare favorably with the RSL curve and with the local deglaciation chronology. These data  
37 demonstrate the utility of *in situ* <sup>14</sup>C to accurately date ice sheet deglaciation, and durations of  
38 postglacial exposure, in regions where cosmogenic <sup>10</sup>Be and <sup>26</sup>Al routinely return complex exposure  
39 results.

## 40 1. Introduction

41 The pacing of retreat of ice sheets in North America and Eurasia since their maximum expansion  
42 during the last glaciation remains an active research field (e.g., Hughes et al., 2016; Stroeven et al.,  
43 2016; Patton et al., 2017; Dalton et al., 2020, 2023). Understanding the triggers and processes causing  
44 the demise of these ephemeral ice sheets yields the best blueprint for understanding the future  
45 behavior of the Greenland and Antarctic ice sheets in a warming climate. Coupling the behavior of  
46 deglaciating ice sheets over the course of the Late Glacial and early Holocene to increasingly precise  
47 climate reconstructions, ~~including and~~ climatic events, requires increased precision in ice sheet  
48 reconstructions (e.g., Bradwell et al., 2021). ~~Increased precision can be achieved enhanced through a~~  
49 ~~coupling of~~ geomorphological mapping of ice sheet margins (such as moraines, grounding zone  
50 wedges, lateral meltwater channels, and ice-dammed lake shorelines and spillways) with numerical  
51 field constraints from a diverse array of dating techniques (e.g., Stroeven et al., 2016; Bradwell et al.,  
52 2021; Regnéll et al., 2023).

53 Ice sheet reconstructions, especially in North America, have ~~attained a high level of detail become~~  
54 ~~highly detailed~~ through radiocarbon dating (Dyke et al., 2002; Dalton et al., 2020). With the advance of  
55 offshore imaging of glacial geomorphology (Greenwood et al., 2017, 2021; Bradwell et al., 2021),  
56 radiocarbon dating has received a renewed upswing in recent years (e.g., Dalton et al., 2020; Bradwell  
57 et al., 2021). However, large ~~tracts of landscape areas~~ lack radiocarbon age constraints on ice sheet  
58 retreat ~~simply due to because of an absence lack~~ of datable organic material. Fortunately, optically-  
59 stimulated luminescence ages on buried sand layers (e.g., Alexanderson et al., 2022) and cosmogenic  
60 nuclide apparent exposure ages on exposed bedrock and erratics have narrowed some of the gaps  
61 (e.g., Hughes et al., 2016; Stroeven et al., 2016; Dalton et al., 2023). In studies using cosmogenic  
62 nuclides, an 'apparent' exposure age is derived from a simple calculation from the nuclide  
63 concentration under consideration (Lal, 1991; Gosse and Phillips, 2001). ~~However, C~~correctly  
64 interpreting the exposure age relies on modelling that considers geological factors that can reduce the  
65 nuclide concentration relative to the time since initial subaerial exposure (such as erosion and burial by  
66 glacial ice, water, snow, and/or soil; Gosse and Phillips, 2001; Schildgen et al., 2005; Ivy-Ochs and  
67 Kober, 2008). Exposure dating is the only technique available in regions where ice sheet erosion has  
68 left the surface bare or covered by a thin drape of till. Kleman et al. (2008) show that for Fennoscandia,

69 these conditions are widespread in coastal regions where ice accelerated towards its streaming sectors  
70 and where wave wash during glacial rebound further thinned or removed pre-existing sediment  
71 covers.

72 Coastal sectors in formerly glaciated regions provide sites important to the study of paleoglaciology.  
73 They offer an abundance of bedrock exposures from which patterns and processes of subglacial  
74 erosion can be studied through cosmogenic nuclide exposure dating (e.g., Hall et al., 2020). Also,  
75 because of the interplay with postglacial sea level, coastal areas yield data on glacioisostatic rebound  
76 that are critical to geodynamic modelling of Earth rheology and thicknesses of former ice sheets (e.g.,  
77 Lambeck et al. (1998, 2010) and Patton et al. (2017), for Fennoscandian examples). Geodynamic  
78 models require validation against measurements of vertical crustal motion (Steffen and Wu, 2011),  
79 such as those provided by recent global positioning system (GPS) measurements (e.g., Lidberg et al.,  
80 2010) and postglacial records of crustal rebound afforded by relative sea level (RSL) curves (e.g., Pässe  
81 and Andersson, 2005). The construction of RSL curves, detailing the history of land surface emergence  
82 from sea level, is traditionally done using either sediments accumulated in isolation basins at different  
83 elevations above sea level or by dating uplifted gravel beach ridges. Typically, isolation basins, and their  
84 sediments, show a progression from marine, to brackish, and finally to freshwater environments as  
85 ~~their bedrock sills they~~ are uplifted through tidal levels (Long et al., 2011). Histories of land uplift above  
86 sea level are documented using micro- and macrofossil analyses of isolation basin sediments and  
87 radiocarbon dating on macrofossils (Romundset et al., 2011). Uplifted beach ridges can be radiocarbon  
88 dated from a variety of materials (Blake, 1993) but most confidently from driftwood, whalebone, and  
89 shells (e.g., Dyke et al., 1992). Gravel beach ridges have also been investigated using OSL and  $^{10}\text{Be}$   
90 exposure dating even though, other than the highest beach ridge, they may be prone to clast  
91 reworking (Briner et al., 2006; Simkins et al., 2013; Bierman et al., 2018). A distinct advantage of  
92 constructing RSL curves using cosmogenic nuclides is that land surface emergence above sea level may  
93 be additionally dated from boulders (Briner et al., 2006) or bedrock (Bierman et al., 2018).

94 The potential for cosmogenic surface exposure dating of last ice sheet retreat in recently glaciated low-  
95 relief cratonic landscapes would seemingly be high because of the frequent outcropping of glacially  
96 sculptured quartz-bearing crystalline bedrock. However, the ice sheet may have been either non-  
97 erosive or erosion was insufficiently deep to remove all the cosmogenic nuclide inventory from  
98 previous exposure periods. Apparent ages are therefore often older than indicated by radiocarbon  
99 dating (Heyman et al., 2011; Stroeven et al., 2016) because they include a component of nuclide  
100 inheritance. Apparent ages younger than indicated by radiocarbon dating can also occur if sampled  
101 rock surfaces have been shielded, for example by sediments, following deglaciation. Concentrations of  
102  $^{10}\text{Be}$  and  $^{26}\text{Al}$ , in either bedrock or erratic boulders, ~~therefore~~ often reflect complex exposure histories  
103 rather than simple deglacial exposure durations (Heyman et al., 2011; Stroeven et al., 2016).

104 In this study we use  $^{14}\text{C}$  produced *in situ* in quartz-bearing bedrock (*in situ*  $^{14}\text{C}$ ) because it potentially  
105 circumvents an overt reliance on the need for deep erosion (>3 m) to remove the inherited signal from  
106 previous exposure periods (Gosse and Phillips, 2001). ~~The reason for this is that, B~~because of its short  
107 half-life of  $5700 \pm 30$  years, ~~nuclide inherited *in situ*  $^{14}\text{C}$  can~~ will ~~have largely decayed away~~ if ice sheet  
108 burial at investigated sites during the last glacial phase (marine isotope stage 2; MIS2) exceeded 25-30  
109 ka, that is, ca. 5 half-lives (Briner et al., 2014).

110 Some studies assessing changes in glacier and ice sheet extents over Late Glacial to Holocene  
111 timescales have used *in situ*  $^{14}\text{C}$  (Miller et al., 2006; Fogwill et al., 2014; Hippe et al., 2014;  
112 Schweinsberg et al., 2018; Pendleton et al., 2019; Young et al., 2021; Schimmelpfennig et al., 2022). In  
113 ~~such these~~ studies, *in situ*  $^{14}\text{C}$  has been applied with other nuclides with longer half-lives, in particular  
114  $^{10}\text{Be}$ , to unravel complex histories of glacier advance and retreat (e.g., Goehring et al., 2011) and  
115 spatial patterns in glacial erosion in mountainous terrain (e.g., Steinemann et al., 2021). ~~However,~~  
116 ~~E~~extensive regions formerly covered by ice sheets are characterized by low relief, ~~and~~ low elevation  
117 terrain. ~~I~~and the effectiveness of *in situ*  $^{14}\text{C}$  in dating ice sheet retreat in these non-alpine settings and  
118 in quantifying shoreline displacement from bedrock samples has not been previously assessed. The  
119 aim of this study is therefore to validate the use of  $^{14}\text{C}$  formed *in situ* in bedrock as a reliable  
120 chronometer by evaluating its performance in duplicating (i) a previously-established Holocene RSL  
121 curve based on radiocarbon dating (Hedenström and Risberg, 2003; SKB, 2020) and (ii) the timing of  
122 deglaciation above the highest (post-glacial) shoreline in nearby east-central Sweden according to  
123 reconstructions of deglaciation of the last ice sheet (Hughes et al., 2016; Stroeven et al., 2016).

124

## 125 2. Study Area

126 Our study is focused on a region that includes low elevation, low relief, Forsmark-Uppland and  
127 adjoining higher elevation and relief Dalarna-Gävleborg in east-central Sweden (Fig. 1). This region was  
128 selected because Forsmark is the location of a planned geological repository for spent nuclear fuel  
129 (e.g., SKB 2022). ~~As such, this region has been intensively studied and has a wealth of -and therefore~~  
130 ~~also has abundant~~ geologic data relevant to our study. This includes in-depth analyses of bedrock and  
131 environmental properties, including influences of glacial and postglacial processes (e.g., Lönnqvist and  
132 Hökmark, 2013; Hall et al., 2019; Moon et al., 2020; SKB, 2020).

133 From spatio-temporal ice sheet reconstructions by Kleman et al. (2008), the study area was glaciated  
134 16-20 times for a total duration of c. 330 kyr over the past 1 Ma. The last deglaciation of the study area  
135 is well-constrained by two recent reconstructions that differ in their approach (Hughes et al., 2016;  
136 Stroeven et al., 2016). The Hughes et al. (2016) reconstruction ~~is explicitly based~~ relies primarily upon  
137 ~~on~~ chronological constraints supplied from radiocarbon, thermal luminescence, optically stimulated

138 [luminescence \(OSL\), infrared stimulated luminescence, electron spin resonance, terrestrial cosmogenic](#)  
139 [nuclide \(TCN\), and U-series dating. Published landform data, mostly with respect to end moraines and](#)  
140 [generally accepted correlations of ice-margin positions between individual moraines, provide](#)  
141 [complementary evidence.](#) ~~but~~ [In contrast,](#) the Stroeven et al. (2016) reconstruction combines  
142 geomorphological constraints for ice sheet margin outlines, [including ice-marginal depositional](#)  
143 [landforms and meltwater channels, ice-dammed lakes, eskers, lineations, and striae,](#) -with  
144 chronological constraints [supplied by radiocarbon, varve, OSL, and TCN dating.](#) Whereas Hughes et al.  
145 (2016) reconstruct ice sheet retreat every 1 ka, and for every ice margin plot its position as “most  
146 credible”, “min”, and “max”, Stroeven et al. (2016) present ice margin positions for every 100 years  
147 inside the Younger Dryas standstill position (Stroeven et al., 2015). These marginal positions are  
148 temporally and spatially defined by the “Swedish Time Scale” clay varve record along the Swedish east  
149 coast (De Geer, 1935, 1940; Strömberg, 1989, 1994; Brunnberg, 1995; Wohlfarth et al., 1995). From  
150 Stroeven et al. (2016), the last deglaciation of the study area occurred  $10.8 \pm 0.3$  ka BP, which overlaps  
151 the timing of deglaciation of the study area from Hughes et al. (2016), within uncertainty (Fig. 1). The  
152 highest postglacial shoreline in east-central Sweden is located at a present elevation of ~200 m a.s.l. in  
153 Dalarna-Gävleborg, ~100 km west of Forsmark (SGU, 2015). The exposure duration of bedrock above  
154 the highest postglacial shoreline ~~therefore~~ represents the time since local deglaciation. Hence, *in situ*  
155  $^{14}\text{C}$  ages from bedrock above the highest postglacial shoreline should conform to the reconstructed  
156 deglaciation age of  $10.8 \pm 0.3$  ka from Stroeven et al. (2016).

157 Below the highest postglacial shoreline, in the Forsmark-Uppland region, the last deglaciation  
158 occurred in a marine environment and the landscape has progressively emerged above sea level  
159 through postglacial isostatic uplift. A RSL curve constructed from radiocarbon dating of basal organic  
160 sediments trapped in isolation basins along elevation transects describes the progressive emergence  
161 of the Forsmark-Uppland landscape above sea level (Robertsson and Persson, 1989; Risberg, 1999;  
162 Bergström, 2001; Hedenström and Risberg, 2003; Berglund, 2005; SKB, 2020). Ages calculated from *in*  
163 *situ*  $^{14}\text{C}$  from bedrock outcrops along an elevation transect would then mirror the Forsmark RSL curve  
164 for their corresponding elevations (but be slightly older because of nuclide production through  
165 shallow water before emergence).

166 A potential complication to the accurate exposure age dating of bedrock surfaces using *in situ*  $^{14}\text{C}$  in  
167 east-central Sweden is that the most recent period of ice sheet burial may not have been sufficiently  
168 long to decay ~~the any~~ *in situ*  $^{14}\text{C}$  inventory inherited from ~~preceding prior~~ exposure. Here, the extent of  
169 the Fennoscandian Ice Sheet during interstadial MIS3 and the timing of ice advance across the  
170 Forsmark region during late MIS3 are crucially important. Kleman et al. (2020) have identified ice-free  
171 conditions around Idre (330 km NW, up-ice, of our study area; Fig. 1) between 55 ka and 35 ka, which  
172 implies inundation of our study area by ice after 35 ka. Combined with a well-constrained final

173 deglaciation age of  $10.8 \pm 0.3$  ka (Stroeven et al. 2016), it appears that our study area has most recently  
174 (during MIS2) been inundated by glacial ice for at most 24 ka. This inference is in line with results from  
175 ice sheet modelling indicating a 22 kyr duration of ice-cover at Forsmark during MIS2 (SKB, 2020).  
176 Consequently, it is possible that *in situ*  $^{14}\text{C}$  concentrations may reflect subaerial exposure of bedrock in  
177 our study area during MIS3 in addition to Holocene exposure, resulting in an offset towards older ages  
178 relative to the RSL curve for Forsmark (Hedenström and Risberg, 2003; SKB, 2020) and the deglaciation  
179 chronologies of Hughes et al. (2016) and Stroeven et al. (2016).

180

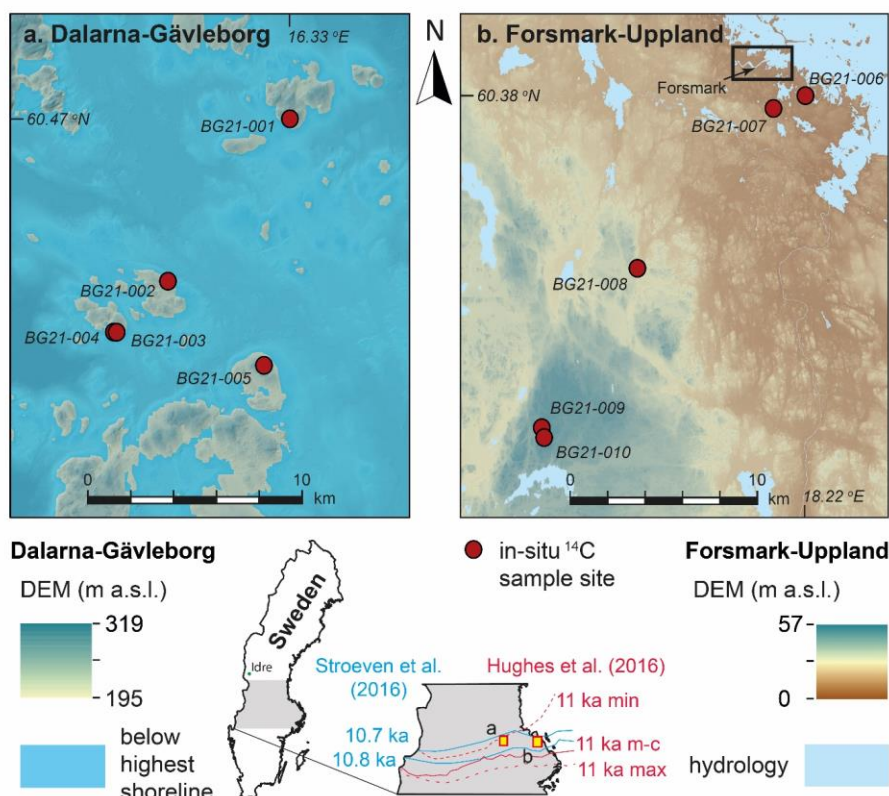
### 181 3. Methods

#### 182 3.1. Sampling of bedrock outcrops for *in situ* $^{14}\text{C}$ measurement

183 We used the following sampling strategy to evaluate the accuracy of bedrock exposure ages derived  
184 from *in situ*  $^{14}\text{C}$  against the Forsmark RSL curve and the deglaciation of the last ice sheet in east-central  
185 Sweden. A rigorous scheme was applied to ensure that we avoided sampling quartz altered through  
186 hydrothermal processes that is likely to occur in major pegmatite intrusions, outcrops located in major  
187 deformation zones, and outcrop-scale veins, fractures, and adjacent rock volumes. Consequently,  
188 sampling was done on outcrops of metagranitoid from the early-Svecokarelian GDG-GSDG suite that  
189 dominates the Bergslagen lithotectonic unit (Stephens and Jansson, 2020). A petrological examination  
190 using transmitted light polarization microscopy was applied to thin sections to ascertain that the quartz  
191 was unlikely to contain multi-fluid phase, vapour phase, or solid-phase inclusions. All samples were  
192 collected using an angle grinder, which permits sampling of hard crystalline bedrock isolated from  
193 outcrop edges, fractures, and quartz veins, and consistently limits sample thicknesses to 3 cm.

194 We collected a total of ten samples for *in situ*  $^{14}\text{C}$  analyses. Five of these were collected along a SW-NE  
195 transect near Forsmark (Fig. 1b). These outcrops were chosen because they span an elevation gradient  
196 of 9.4–56.0 m a.s.l. and exposure ages derived from *in situ*  $^{14}\text{C}$  can therefore be evaluated against the  
197 Forsmark RSL curve. We collected a further five samples from locations above the highest shoreline (Fig.  
198 1a) to determine the age of local deglaciation for comparison with published deglaciation chronologies  
199 (Hughes et al., 2016; Stroeven et al., 2016). Sample locations were logged on a 2 m-resolution LiDAR  
200 digital elevation model (DEM) displayed in ArcGIS 10 on a tablet computer. A GPS add-in tool in ArcGIS  
201 10 was used to record positional data, within a horizontal precision of 2 m. The elevation of each sample  
202 location was extracted from the DEM and has a precision of tens of centimetres. The influence of these  
203 minor positional uncertainties on our  $^{14}\text{C}$  calculations is trivial and none of the sample sites is influenced  
204 by topographic shielding that could reduce the accumulation of  $^{14}\text{C}$  in bedrock.

205 Each sampled bedrock outcrop formed a local topographic high, which minimizes the risk of burial by  
 206 soil and snow (Supplement 1). Moss mats were present on all sampled outcrops. Although we avoided  
 207 sampling bedrock that was moss-covered, we cannot be certain that moss mats did not formerly cover  
 208 the sample sites. Given a compressed thickness of 0.5 cm and an estimated density of  $0.7 \text{ g/cm}^3$ , this  
 209 may have contributed to a shielding of the sampled rock surfaces of  $0.35 \text{ g/cm}^2$ , which is negligible and  
 210 is therefore excluded from our age inferences.



211

212 **Figure 1.** Sample locations for *in situ*  $^{14}\text{C}$  dating in (a) Dalarna-Gävleborg and (b) Forsmark-Uppland. The  
 213 five Dalarna-Gävleborg sample sites are located on what were islands above the highest postglacial  
 214 shoreline (shown), whereas the five sample sites from Forsmark-Uppland are located below the highest  
 215 shoreline (not shown because the entire area was submerged). See inset maps for locations of panels a  
 216 and b and for the 10.7 ka BP and 10.8 ka BP retreat isochrones (blue) from Stroeven et al. (2016) and 11  
 217 ka BP (most-credible, minimum, and maximum) retreat isochrones (red) from Hughes et al. (2016). The  
 218 rectangle in panel b approximately indicates the site selected for the planned geological repository for  
 219 spent nuclear fuel at Forsmark. DEM with 2 m resolution, from LiDAR data, Lantmäteriet.

### 220 3.2. Laboratory preparation for accelerator mass spectrometry (AMS)

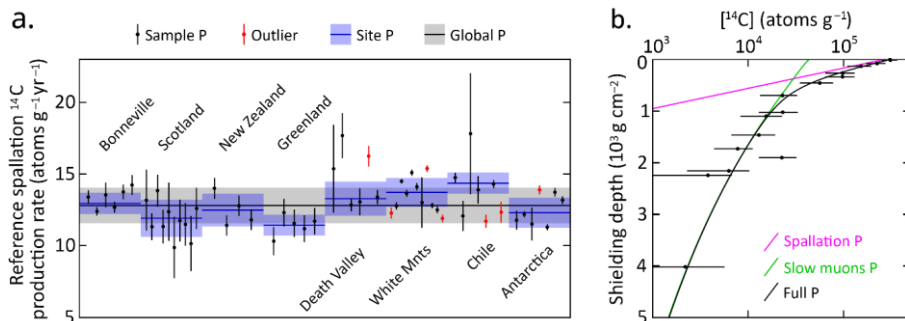
221 Samples were physically and chemically processed at the Purdue Rare Isotope Measurement Laboratory  
222 (PRIME Lab) at Purdue University, U.S.A. Concentrations of *in situ* <sup>14</sup>C were determined from purified  
223 quartz separates through automated procedures (Lifton et al., 2023). Approximately 5 g of quartz from  
224 each sample was added to a degassed LiBO<sub>2</sub> flux in a re-usable 90% Pt/10% Rh sample boat and heated  
225 to 500 °C for one hour in ca. 6.7 kPa of Research Purity O<sub>2</sub> to remove atmospheric contaminants, which  
226 were discarded. The sample was then heated to 1100 °C for three hours to dissolve the quartz and  
227 release the *in situ* <sup>14</sup>C, again in an atmosphere of ca. 6.7 kPa of Research Purity O<sub>2</sub> to oxidize any evolved  
228 carbon species to CO<sub>2</sub>. The CO<sub>2</sub> from the 1100 °C step was then purified, measured quantitatively, and  
229 converted to graphite for <sup>14</sup>C AMS measurement at PRIME Lab (Lifton et al., 2023). To test for data  
230 reproducibility, sample BG21-002 was randomly selected to undergo laboratory preparation and AMS a  
231 second time. Measured concentrations of *in situ* <sup>14</sup>C are calculated from the measured isotope ratios via  
232 AMS following Hippe and Lifton (2014) ([Table 1](#)).

### 233 3.3. Exposure age calculations

234 The expage calculator version 202403312 (<http://expage.github.io/calculator>) is used to calculate  
235 apparent exposure ages. It is based on the original CRONUS calculator v. 2 (Balco et al., 2008), the LSDn  
236 production rate scaling (Lifton et al., 2014), and the CRONUScalc calculator (Marrero et al., 2016), using  
237 the geomagnetic framework of Lifton (2016) with the SHA.DIF.14k model for the last 14 kyr. Exposure  
238 ages are calculated using resulting time-varying <sup>14</sup>C production rates accounting for decay and  
239 interpolated to match the measured <sup>14</sup>C concentration. The production rate from muons is calibrated  
240 against the Leymon High core <sup>14</sup>C data of Lupker et al. (2015) and the production rate from spallation is  
241 calibrated against updated global <sup>14</sup>C production rate calibration data (Schimmelpfennig et al., 2012;  
242 Young et al., 2014; Lifton et al., 2015; Borchers et al., 2016; Phillips et al., 2016; Koester and Lifton, 2023,  
243 [corrigendum in prep](#)). This calibration is done iteratively for spallation and muons to reach convergence,  
244 using the expage production rate calibration methods (Fig. 2).

245 Exposure age calculations along the Forsmark-Uppland transect account for <sup>14</sup>C production during  
246 emergence through shallow water. ~~However, B~~burial of sampled surfaces by snow is excluded from the  
247 age calculations for all sample sites because we neither know how snow burial depths and durations  
248 vary between sites nor vary through time. The effect of snow burial would be to slightly decrease  
249 cosmogenic nuclide production in the underlying rock surface (Schildgen et al., 2005) and we have  
250 minimized this effect through our sampling strategy.





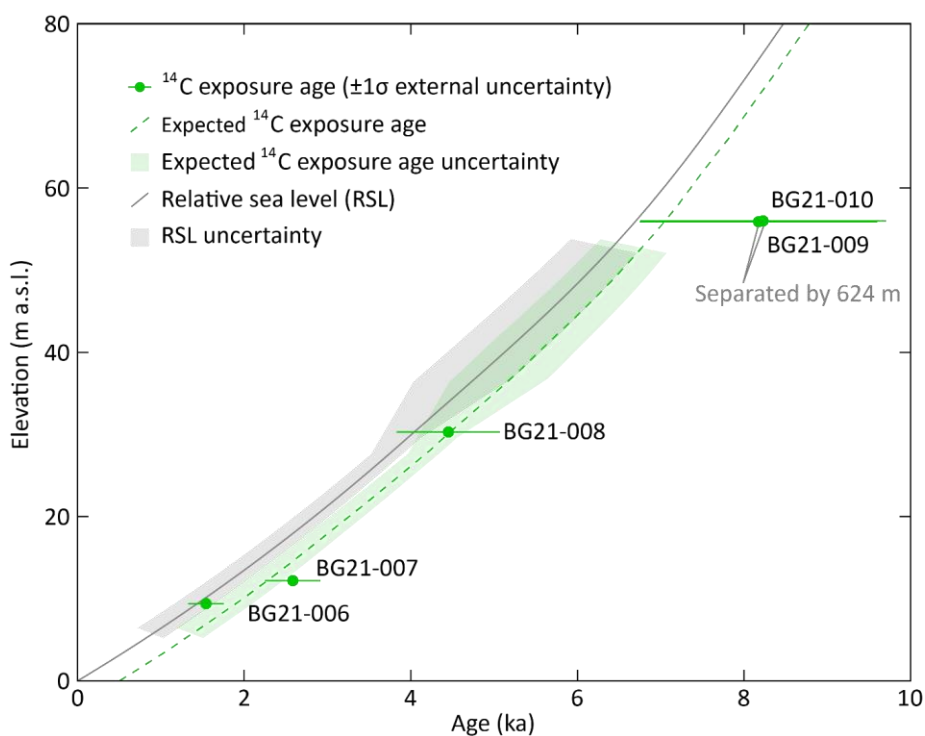
251 **Figure 2.** Production rate calibration of  $^{14}\text{C}$  in quartz. **(a)** Reference spallation  $^{14}\text{C}$  production rate  
 252 calibration based on data from Schimmelpfennig et al. (2012), Young et al. (2014), Lifton et al. (2015),  
 253 Borchers et al. (2016), and Phillips et al. (2016), corrected per Hippe and Lifton (2014) and compiled in  
 254 Koester and Lifton (2023). An uncertainty-weighted production rate is calculated for each of the eight  
 255 sites. Outliers, which are not included in the uncertainty-weighted production rates, are determined  
 256 based on the requirement that there should be at least three samples yielding a reduced chi-square  
 257 statistic ( $\chi^2_R$ ) with a p-value of at least 0.05 for the assumption that the individual production rates from  
 258 a site are derived from one normal distribution. For  $\chi^2_R$ , but not the uncertainty-weighting, we use the  
 259 largest of the sample-specific production rate uncertainty based on the  $^{14}\text{C}$  concentration uncertainties  
 260 and 5% of the sample production rate. This procedure does not punish samples with low measurement  
 261 uncertainties, which otherwise risk exclusion as outliers. We adopt a global reference spallation  $^{14}\text{C}$   
 262 production rate of  $13.35 \pm 1.25$  atoms  $\text{g}^{-1} \text{yr}^{-1}$ , calculated as the arithmetic mean of the eight  
 263 site production rates with the uncertainty being based on an uncertainty-weighted deviation of all  
 264 included single sample production rates, excluding outliers. **(b)** Calibration of  $^{14}\text{C}$  production rate from  
 265 muons based on the data of Lupker et al. (2015). The calibration is based on the method used in the  
 266 CRONUScalc calculator (Marrero et al., 2016; Phillips et al., 2016). The figure shows the best fit  $^{14}\text{C}$   
 267 concentration profiles produced from spallation, slow muons, and full production. The best fit yields  
 268 near zero production from fast muons (cf. Lupker et al., 2015). The production rate calibration has been  
 269 carried out using the expage-202403306 calculator in an iterative way to make the global reference  
 270 spallation  $^{14}\text{C}$  production rate converge with the production rate from muons.

271

#### 272 4. Results

273 Analytical results for *in situ*  $^{14}\text{C}$  samples and procedural blanks are presented in Table 1. The mean and  
 274 standard deviation are used to correct measured  $^{14}\text{C}$  sample inventories (Table 1) because procedural  
 275 blanks are well-constrained during the analytical time frame. Inferred ages for the five *in situ*  $^{14}\text{C}$  samples  
 276 from the Forsmark-Upland transect (i.e., below the highest postglacial shoreline) are shown relative to

277 the Holocene RSL curve for Forsmark and the expected *in situ*  $^{14}\text{C}$  exposure age curve considering  
 278 subaqueous cosmogenic nuclide production (Figure 3; Tables 1 and 2). Exposure age uncertainties are  
 279 large with internal uncertainties (measurement uncertainties; Balco et al., 2008) of 5-9% and external  
 280 uncertainties of 12-25% (also including production rate uncertainties, which are high relative to  
 281  $^{10}\text{Be}$  (Borchers et al., 2016; Phillips et al., 2016)). Apparent exposure ages increase consistently with  
 282 elevation and match expected ages within uncertainty. The two highest samples have near-identical  
 283 apparent exposure ages and elevations. However, these samples provide independent ages because  
 284 they are horizontally separated by 624 m (Figure 1b). There is good agreement between ages inferred  
 285 from these *in situ*  $^{14}\text{C}$  data and the RSL curve constructed from organic radiocarbon dating of isolation  
 286 events (Hedenström and Risberg, 2003; SKB, 2020).

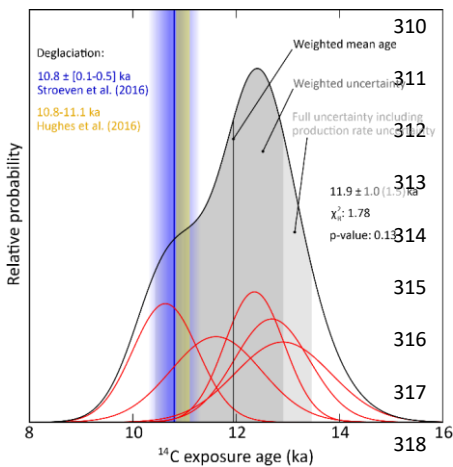


287

288 **Figure 3.** Apparent  $^{14}\text{C}$  exposure ages for five Forsmark samples from below the highest shoreline (Fig.  
 289 1b; Table 2) with  $1\sigma$  external uncertainties. The expected exposure ages are calculated assuming the RSL  
 290 curve is correct, the  $^{14}\text{C}$  spallation production rate is correct, partial exposure as the sample approaches  
 291 the water surface, and full post-glacial exposure for the duration above sea level. Hence, the expected  
 292 exposure age curve is a few hundred years older than the RSL curve. The RSL curve is from SKB (2020)  
 293 and uncertainties for the 1–6 ka interval are calculated from the original radiocarbon data in Hedenström

294 and Risberg (2003). The RSL uncertainty envelope is also transposed onto the expected exposure age  
 295 curve.

296 Apparent exposure ages for the five *in situ* <sup>14</sup>C samples located above the highest shoreline in Dalarna  
 297 and Gävleborg (Fig. 1a) are shown in Figure 4 and Table 2. The weighted mean age from all five samples  
 298 is  $11.92 \pm 1.53$  ka. These data display a  $\chi^2_R$  of 1.78 and a p-value of 0.13 based on  $1\sigma$  internal uncertainties  
 299 (Fig. 4a), which does not support a rejection of the hypothesis that the apparent exposure ages represent  
 300 the same population. In addition to the samples being from the same population, the exposure ages are  
 301 consistent, within uncertainty, with the expected deglaciation age of  $10.8 \pm 0.3$  ka (Stroeven et al. 2016).  
 302 Replicate measurements on sample BG21-002 closely agree and an age based on a weighted mean <sup>14</sup>C  
 303 concentration is shown in Figure 4. ~~Sample BG21-001 provides the youngest apparent age but, because~~  
 304 ~~this sample was from a low profile outcrop (Supplement 1), this age may reflect partial shielding of the~~  
 305 ~~sampled bedrock surface by a past shallow soil cover or perhaps a deeper snow cover than the other~~  
 306 ~~sites. We therefore consider this sample as least likely to provide a reliable age. Removing this sample~~  
 307 ~~from consideration indicates that the remaining four sample sites are more clustered, with an older~~  
 308 ~~weighted mean age of  $11.6124 \pm 1.31$  ka, which displays a  $\chi^2_R$  of 0.423 and a p value of 0.743 based on~~  
 309  ~~$1\sigma$  internal uncertainties (Fig. 4b).~~



319 **Figure 4.** ~~Summed Probability density plots~~ Normalized kernel density estimates of the  
 320 exposure ages from samples above the highest shoreline (Fig. 1a; Table 2). The individual samples (red  
 321 curves) display  $1\sigma$  internal uncertainty (measurement uncertainty). For the repeat sample BG21-002,  
 322 the exposure age is calculated with a weighted mean <sup>14</sup>C concentration using a 2% uncertainty. ~~(a) The~~  
 323 ~~probability density and data for all five samples. For the full set of samples, the~~ cosmogenic nuclide  
 324 ages yield a reduced chi-square ( $\chi^2_R$ ) of 1.78 and a p-value of 0.13 based on internal uncertainties, which  
 325 indicates that they are from the same population. ~~(b) The probability density and data with sample~~

326 ~~BG21-001 excluded as an outlier. These cosmogenic nuclide ages yield a  $\chi^2_\nu$  of 0.423 and a p value of~~  
327 ~~0.743 based on internal uncertainties, which again indicate that they are from the same population. All~~  
328 ~~ages are referenced to the sampling year 2021. The weighted ages of  $11.92 \pm 1.53$  ka and  $11.612.4 \pm$~~   
329  ~~$1.31$  ka both overlap with the deglaciation age from Stroeven et al. (2016).~~

Formatted Table

Table 1. Extraction and measurement details

Sample ID	PCEGS #	PLID <sup>a</sup>	PLID <sup>b</sup>	Mass Quant <sup>c</sup> (g)	C yield (μg)	Diluted mass C (μg)	AMS Split Mass C (μg)	AMS Split Mass C <sup>d</sup> (μg)	δ <sup>13</sup> C (‰)	<sup>14</sup> C/ <sup>12</sup> C (10 <sup>-12</sup> )	<sup>14</sup> C/C <sub>meas</sub> (10 <sup>-12</sup> )	<sup>14</sup> C (10 <sup>6</sup> at)	<sup>14</sup> C (10 <sup>6</sup> at g <sup>-1</sup> ) <sup>e</sup>
BG21-001	146	202101960	54	5.0 ± 0.1	303.8 ± 3.4	303.8 ± 3.4	303.8 ± 3.4	303.8 ± 3.4	-45.9 ± 0.2	0.3390 ± 0.0075	0.3412 ± 0.0079	0.6177 ± 0.0179	1.2296 ± 0.0357
BG21-002	147	202101961	54	7.8 ± 0.1	303.3 ± 3.3	303.3 ± 3.3	303.3 ± 3.3	303.3 ± 3.3	-44.8 ± 0.2	0.4555 ± 0.0096	0.4623 ± 0.0102	0.6470 ± 0.0181	1.2879 ± 0.0360
BG21-003	148	202101962	54	17.6 ± 0.3	303.4 ± 3.3	303.4 ± 3.3	303.4 ± 3.3	303.4 ± 3.3	-43.9 ± 0.2	0.4693 ± 0.0108	0.4709 ± 0.0113	0.6604 ± 0.0197	1.3180 ± 0.0393
BG21-002R	150	202201473	54	7.7 ± 0.1	305.3 ± 3.3	305.3 ± 3.3	305.3 ± 3.3	305.3 ± 3.3	-45.2 ± 0.2	0.4568 ± 0.0135	0.4624 ± 0.0142	0.6519 ± 0.0237	1.2931 ± 0.0470
BG21-004	152	202101963	54	11.9 ± 0.2	305.7 ± 3.3	305.7 ± 3.3	305.7 ± 3.3	305.7 ± 3.3	-44.6 ± 0.2	0.4618 ± 0.0079	0.4601 ± 0.0083	0.6630 ± 0.0150	1.3105 ± 0.0314
BG21-005	153	202101964	54	4.6 ± 0.1	304.5 ± 3.3	304.5 ± 3.3	304.5 ± 3.3	304.5 ± 3.3	-45.4 ± 0.2	0.4600 ± 0.0127	0.4667 ± 0.0134	0.6568 ± 0.0225	1.2935 ± 0.0444
BG21-006	155	202101965	54	5.5 ± 0.1	306.8 ± 3.7	306.8 ± 3.7	306.8 ± 3.7	306.8 ± 3.7	-45.2 ± 0.2	0.4277 ± 0.0066	0.4172 ± 0.0059	0.1243 ± 0.0101	0.2453 ± 0.0189

Table 1. *In situ* <sup>14</sup>C sample measurement details

Sample	PCEGS <sup>1</sup> #	PLID <sup>2</sup>	Mass Quant <sup>3</sup> (g)	C yield <sup>4</sup> (μg)	Diluted Mass C <sup>5</sup> (μg)	AMS Split Mass C <sup>6</sup> (μg)	δ <sup>13</sup> C (‰ VPDB) <sup>7</sup>	<sup>14</sup> C/ <sup>12</sup> C (10 <sup>-12</sup> ) <sup>8</sup>	<sup>14</sup> C/C <sub>meas</sub> <sup>9</sup> (10 <sup>-12</sup> )	<sup>14</sup> C (10 <sup>6</sup> at) <sup>10</sup>	[ <sup>14</sup> C] (10 <sup>6</sup> at g <sup>-1</sup> ) <sup>11</sup>
BG21-001	PCEGS-146	202101960	5.02378	5.0 ± 0.1	393.8 ± 4.8	382.3 ± 4.6	-45.9 ± 0.2	3.3992 ± 0.0745	3.4118 ± 0.0785	6.1771 ± 0.1793	1.2296 ± 0.0357
BG21-002	PCEGS-147	202101961	5.02383	7.8 ± 0.1	303.3 ± 3.7	294.4 ± 3.6	-44.8 ± 0.2	4.5548 ± 0.0964	4.6226 ± 0.1016	6.4703 ± 0.1806	1.2879 ± 0.0360
BG21-002R	PCEGS-150	202201473	5.04116	7.7 ± 0.1	305.3 ± 3.7	296.4 ± 3.6	-45.2 ± 0.2	4.5575 ± 0.1350	4.6239 ± 0.1422	6.5186 ± 0.2368	1.2931 ± 0.0470
BG21-003	PCEGS-148	202101962	5.01070	17.6 ± 0.3	303.4 ± 3.7	294.5 ± 3.6	-43.9 ± 0.2	4.6325 ± 0.1075	4.7091 ± 0.1134	6.6042 ± 0.1969	1.3180 ± 0.0393
BG21-004	PCEGS-152	202101963	5.05927	11.9 ± 0.2	305.7 ± 3.7	296.8 ± 3.6	-44.6 ± 0.2	4.6181 ± 0.0789	4.6905 ± 0.0832	6.6300 ± 0.1588	1.3105 ± 0.0314
BG21-005	PCEGS-153	202101964	5.07578	4.6 ± 0.1	304.5 ± 3.7	295.6 ± 3.6	-45.4 ± 0.2	4.5997 ± 0.1272	4.6688 ± 0.1339	6.5656 ± 0.2251	1.2935 ± 0.0444
BG21-006	PCEGS-155	202101965	5.06572	5.5 ± 0.1	306.8 ± 3.7	297.8 ± 3.6	-45.2 ± 0.2	1.2766 ± 0.0562	1.1715 ± 0.0594	1.2426 ± 0.1010	0.2453 ± 0.0199
BG21-007	PCEGS-157	202101966	5.03589	6.9 ± 0.1	309.2 ± 3.8	300.1 ± 3.7	-45.0 ± 0.2	1.6838 ± 0.0507	1.6007 ± 0.0536	1.9221 ± 0.0960	0.3817 ± 0.0191
BG21-008	PCEGS-158	202101967	5.07653	4.0 ± 0.1	308.9 ± 3.8	299.9 ± 3.6	-45.4 ± 0.2	2.3565 ± 0.0634	2.3076 ± 0.0669	3.0145 ± 0.1185	0.5938 ± 0.0234
BG21-009	PCEGS-160	202101968	5.01906	55.3 ± 0.7	305.6 ± 3.7	296.6 ± 3.6	-38.0 ± 0.2	3.3393 ± 0.0946	3.3681 ± 0.1005	4.6013 ± 0.1703	0.9168 ± 0.0339
BG21-010	PCEGS-161	202101969	4.99961	42.2 ± 0.6	306.0 ± 3.7	297.0 ± 3.6	-40.1 ± 0.2	3.3197 ± 0.0680	3.3399 ± 0.0721	4.5648 ± 0.1321	0.9130 ± 0.0284
<b>Procedural Blanks</b>											
PB2-03222022	PCEGS-135	202201450	--	1.4 ± 0.1	305.2 ± 3.7	296.2 ± 3.6	-40.2 ± 0.2	0.4853 ± 0.0298	0.3413 ± 0.0320	0.5222 ± 0.0493	--
PB2-04212022	PCEGS-145	202201452	--	1.8 ± 0.1	307.0 ± 3.7	298.0 ± 3.6	-46.0 ± 0.2	0.5182 ± 0.0273	0.3731 ± 0.0292	0.5742 ± 0.0455	--
PB2-05212022	PCEGS-163	202201454	--	2.3 ± 0.1	307.4 ± 3.7	298.4 ± 3.6	-46.0 ± 0.2	0.5364 ± 0.0315	0.3922 ± 0.0335	0.6045 ± 0.0521	--
PB2-06022022	PCEGS-169	202201459	--	2.3 ± 0.1	307.3 ± 3.7	298.3 ± 3.6	-40.3 ± 0.2	0.4920 ± 0.0291	0.3486 ± 0.0312	0.5371 ± 0.0486	--
										<i>Mean ± 1σ (All blanks)</i>	
										<i>Mean ± 1σ (145, 163 only)</i>	
										<i>0.5894 ± 0.0214</i>	

Notes

- Purdue Carbon Extraction and Graphitization System.
- Prime Lab ID.
- Mass graphitized for AMS analysis after small aliquot (ca. 9 μg C) taken for stable C isotopic analysis offline.
- VPDB is Vienna Pee Dee Belemnite.
- Measured relative to OX-2 standard.
- Corrected for mass-dependent graphitization blank (based on AMS Split Mass C) and stable C composition.
- Sample values calculated using Diluted Mass C and corrected for mean procedural blank (All blanks).

331  
332

Table 2-2. Apparent *in situ* <sup>14</sup>C ages from quartz, Dalarna-Gävleborg and Forsmark-Uppland.

Sample ID	Lat (°)	Long (°)	Elevation (m a.s.l.)	<sup>14</sup> C aAge ± Unc. <sup>Ext.</sup> (± Unc. <sup>Int.</sup> ) <sup>2σ</sup> (ka)
BG21-001	60.47432	16.33134	236.5	10.6 ± 2.2 (± 0.6)
BG21-002	60.40615	16.22197	212.6	12.3 ± 2.9 (± 0.8)
BG21-002R	60.40615	16.22197	212.6	12.4 ± 3.0 (± 1.1)
BG21-003	60.38459	16.17649	216.3	12.9 ± 3.2 (± 0.9)
BG21-004	60.38451	16.17440	217.8	12.7 ± 3.0 (± 0.7)
BG21-005	60.36888	16.30526	248.1	11.6 ± 2.6 (± 0.9)
BG21-006	60.38490	18.22308	9.4	1.5 ± 0.2 (± 0.1)
BG21-007	60.37892	18.19129	12.2	2.6 ± 0.3 (± 0.2)
BG21-008	60.30504	18.04993	30.3	4.5 ± 0.6 (± 0.2)
BG21-009	60.22988	17.94989	56.0	8.2 ± 1.5 (± 0.5)
BG21-010	60.22431	17.95051	55.9	8.2 ± 1.4 (± 0.4)

Notes

1 All samples have a thickness of 3 cm, a density of 2.7 g cm<sup>-3</sup>, and a shielding factor of 1. Zero erosion is assumed.  
2 <sup>14</sup>C aAge and 1σ external uncertainty (1σ internal uncertainty), and Unc.<sup>Ext.</sup> is external uncertainty and Unc.<sup>Int.</sup> is (internal uncertainty). Both are 1σ.

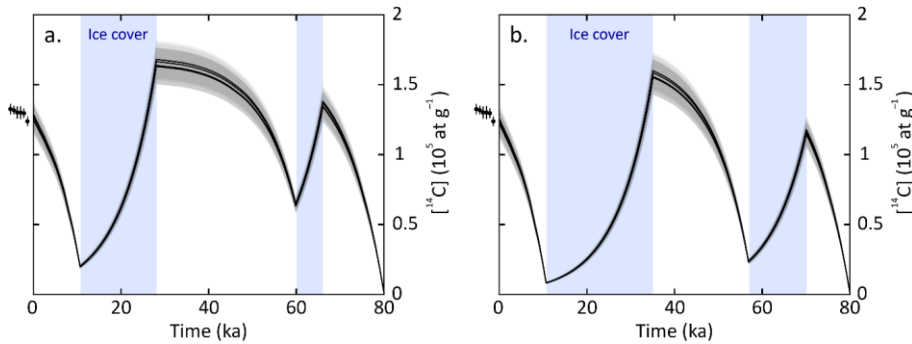
333  
334  
335

## 336 5. Discussion

337 The *in situ* <sup>14</sup>C bedrock exposure ages from the Forsmark-Uppland transect (i.e., below the highest  
338 postglacial shoreline) consistently increase with elevation and overlap the expected exposure age  
339 curve, within uncertainty (Fig. 3). ~~Because the apparent exposure ages accurately reflect the timing of~~  
340 ~~landscape emergence, *in situ* <sup>14</sup>C is indicated as having high potential as a chronometer over Late~~  
341 ~~Glacial Holocene timescales in low relief, low elevation settings.~~ This study adds to precious few  
342 ~~demonstrations of the ability of applications of cosmogenic nuclides isotopes to define~~ <sup>ing</sup> postglacial  
343 landscape emergence above sea level (Briner et al., 2006; Bierman et al., 2018). Briner et al. (2006)  
344 present good (visual) congruence with a record of shoreline emergence built from radiocarbon-dated  
345 driftwood and fauna by Dyke et al. (1992) using <sup>10</sup>Be measurements on boulders in beaches derived  
346 from wave-washed till. Their study also mentions that building a relative sea level curve from pebbles,  
347 cobbles and plucked bedrock suffered from inheritance problems, an experience shared by Matmon et  
348 al. (2003) while attempting the dating of chert on beach ridges in southern Israel and heeded by  
349 Bierman et al. (2018). Bierman et al. (2018) successfully dated landscape emergence on Greenland  
350 using <sup>10</sup>Be across a range of settings, including bedrock below the highest shoreline, cobbles from beach  
351 ridges at the highest shoreline, and boulders and bedrock above the highest shoreline. They note that  
352 success hinges on the requirement of warm-based ice and deep glacial erosion in exposing bedrock  
353 devoid of an inherited cosmogenic nuclide inventory. In many regions, however, including east-central  
354 Sweden and more widely in Fennoscandia, these requirements are not met either because of cold-  
355 based conditions (Patton et al., 2016; Stroeven et al., 2016) or weakly erosive warm-based ice such as  
356 at Forsmark (Hall et al., 2019; SKB, 2020), during all or much of glacial time. Cosmogenic nuclide  
357 inheritance is therefore a part of the landscape fabric. Bierman et al. (2018) advocate the use of *in situ*  
358 <sup>14</sup>C as a methodology to circumvent inheritance problems. Our study is the first to follow-up on that  
359 suggestion, and shows, convincingly, that using *in situ* <sup>14</sup>C can extend the study of landscape rebound  
360 to regions where ice sheet erosion was insufficiently deep to allow for the application of long-lived  
361 nuclides.

362 Five bedrock samples from above the highest postglacial shoreline are well-clustered and the weighted  
363 mean age (and full uncertainty) of  $11.92 \pm 1.53$  ka overlaps with the predicted deglaciation age of  $10.8$   
364  $\pm 0.3$  ka (Fig. 4a; Hughes et al., 2016; Stroeven et al., 2016). ~~Removing the youngest age from~~  
365 ~~consideration results in more strongly clustered ages (Fig. 4b) and an older mean weighted age of~~  
366  ~~$11.612.4 \pm 1.31$  ka, which still overlaps the predicted deglaciation age, within uncertainty. We therefore~~  
367 ~~do not further discriminate between these results.~~ Because derived exposure ages overlap with the  
368 predicted deglaciation age, we further infer that the *in situ* <sup>14</sup>C samples, including those located below  
369 the highest postglacial shoreline, within uncertainty, lack significant inheritance from previous

370 exposure. Model scenarios of *in situ*  $^{14}\text{C}$  concentration evolution over varying durations of MIS2 and  
 371 MIS4 ice cover indicate are consistent with minor inheritance, even with short periods of ice coverage



372 and an assumption of no glacial or interglacial erosion (Figure 5). The apparent lack of inheritance in  
 373 samples from above the highest shoreline implies that the last ice sheet advanced over the study area  
 374 soon after 35 ka, in accordance with previous inferences for Forsmark (SKB, 2020). Even if the last ice  
 375 sheet would have had advanced over the region as late as 28 ka BP, there would only be a very  
 376 minor negligible amount inventory of inherited  $^{14}\text{C}$  atoms produced prior to the MIS2 ice advance. An  
 377 alternative interpretation is that the last ice sheet advanced more recently but that glacial erosion  
 378 during MIS2 was sufficiently deep to remove any nuclide inheritance.

379 **Figure 5.** Modelled *in situ*  $^{14}\text{C}$  concentration evolution over the last 80 kyr in bedrock surfaces through  
 380 alternating periods of subaerial exposure and burial by ice sheets during MIS2 and MIS3. These  
 381 histories are modelled from  $^{14}\text{C}$  concentrations in the five samples (BG21-001–BG21-005) from above  
 382 the highest shoreline, and assume no glacial or interglacial erosion. The  $^{14}\text{C}$  development is modelled  
 383 assuming no glacial or interglacial erosion, continuous exposure to cosmic rays during ice-free periods,  
 384 and full shielding from cosmic rays (no  $^{14}\text{C}$  production) during periods with ice cover. The points just  
 385 left of the plots display the measured  $^{14}\text{C}$  concentrations for the six sample measurements of the  
 386 samples (Table 1). (a) Scenario with short periods of MIS4 and MIS2 ice cover from 66 to 60 ka BP  
 387 and from 28 ka BP to the time of deglaciation around 10.7 ka BP. (b) Scenario with longer periods of  
 388 MIS4 and MIS2 ice cover from 70 to 57 ka BP and from 35 ka BP to the deglaciation around 10.7 ka  
 389 BP. Due to the rapid decay of  $^{14}\text{C}$  (with a half-life of  $5700 \pm 30$  years), both scenarios yield similar  
 390 similar end-point concentrations of  $^{14}\text{C}$  that overlap, within uncertainties, with the measured sample  
 391 concentrations.

392 Our *in situ*  $^{14}\text{C}$  data from above the highest (postglacial) shoreline demonstrate good potential  
 393 for this nuclide to help constrain the deglaciation chronology of former ice sheets. This is especially  
 394 true for regions with thin drift till drapes, abundant bedrock exposures, and sparse moraines outlining



395 successive retreat stages. In Fennoscandia, thin ~~drift tills conditions~~ occur commonly (cf. Kleman et al.,  
396 2008) and ice sheet retreat appears to have proceeded uninterrupted inside the Younger Dryas moraine  
397 belt (apart from the Central Finland Ice-Marginal Formation; e.g., Rainio et al., 1986; Stroeven et al.,  
398 2016). Whereas the post-Younger Dryas deglaciation of east-central Sweden is well constrained by clay-  
399 varve chronology below the highest postglacial shoreline (Strömberg, 1989) ~~below the highest~~  
400 ~~postglacial shoreline~~, there are vast areas above the highest shoreline that remain poorly constrained  
401 by data (Stroeven et al. 2016). In addition to a lack of datable deglacial landforms, this is attributable  
402 to glacial erosion of bedrock having frequently been insufficient to remove inventories of long half-life  
403  $^{10}\text{Be}$  and  $^{26}\text{Al}$  (Patton et al., 2022), thereby leaving nuclides inherited from exposure prior to the last  
404 glaciation (Heyman et al., 2011; Stroeven et al., 2016). Because of the short  $^{14}\text{C}$  half-life and an  
405 improved sampling methodology, *in situ*  $^{14}\text{C}$  may now be a prime candidate nuclide to be included in  
406 last deglaciation studies on glaciated cratons, such as the dating of boulders deposited along glacial  
407 flowlines; a technique practiced successfully using  $^{10}\text{Be}$  (Margold et al., 2019; Norris et al., 2022).

408

## 409 6. Conclusion

410 Ten *in situ*  $^{14}\text{C}$  measurements on bedrock are consistent with a RSL curve for Forsmark derived from  
411 organic radiocarbon dating of basal sediments in isolation basins and the Fennoscandian Ice Sheet  
412 deglaciation chronologies from Stroeven et al. (2016) and Hughes et al. (2016). This study introduces  
413 the use of *in situ*  $^{14}\text{C}$  in Fennoscandian Ice Sheet paleoglaciology and outlines a promise of its use as a  
414 basis for supporting future shoreline displacement studies and for tracking the deglaciation in areas  
415 that lack datable organic material and where  $^{10}\text{Be}$  and  $^{26}\text{Al}$  routinely return complex exposure results.

416

417 **Data availability.** Data are available in Supplements 1-3. LiDAR data used in the study ~~can~~  
418 ~~downloaded are available~~ from <https://www.lantmateriet.se>

419 **Author contributions.** BWG and APS initiated the study, with support from KH and JON, and drafted  
420 the manuscript. BWG, APS, and AL did the sampling. AL did petrological analyses of the sampled  
421 bedrock. NAL completed sample preparation for AMS and provided the results. JH carried out  
422 cosmogenic nuclide production rate and exposure age calculations. MWC oversaw the AMS. All  
423 authors revised the manuscript.

424 **Competing interests.** The contact author has declared that none of the authors has any competing  
425 interests.

426 **Disclaimer.** Publisher's note: Copernicus Publications remains neutral with regard to jurisdictional  
427 claims in published maps and institutional affiliations.

428 **Acknowledgements.** We thank Johan Liakka (SKB) for his support in completing this study and  
429 Nicolás Young and an anonymous reviewer for comments that improved this manuscript.-

430 **Financial support.** This research was supported by the Swedish Nuclear Fuel and Waste Management  
431 Company.

432 **Review statement.** [This paper was edited by Pieter Vermeesch and reviewed by Nicolás Young and](#)  
433 [an anonymous reviewer.](#)

#### 434 **References**

435 Alexanderson, H., Hättstrand, M., Lindqvist, M. A., Sigfusdottir, T.: MIS 3 age of the Veiki moraine in  
436 N Sweden - Dating the landform record of an intermediate-sized ice sheet in Scandinavia, Arctic,  
437 Antarctic, and Alpine Research, 54, 239-261, 2022.

438 Balco, G., Stone, J. O., Lifton, N. A., Dunai, T. J.: A complete and easily accessible means of calculating  
439 surface exposure ages or erosion rates from  $^{10}\text{Be}$  and  $^{26}\text{Al}$  measurements, Quaternary  
440 Geochronology, 3, 174-195, 2008.

441 Berglund, M.: The Holocene shore displacement of Gästrikland, eastern Sweden: a contribution to  
442 the knowledge of Scandinavian glacio-isostatic uplift, Journal of Quaternary Science, 20, 519-531,  
443 2005.

444 Bergström, E.: Late Holocene distribution of lake sediment and peat in NE Uppland, Sweden, SKB R-  
445 01-12, Svensk Kärnbränslehantering AB, 2001.

446 Bierman, P. R., Rood, D. H., Shakun, J. D., Portenga, E. W., Corbett, L. B.: Directly dating postglacial  
447 Greenlandic land-surface emergence at high resolution using *in situ*  $^{10}\text{Be}$ , Quaternary Research, 90,  
448 110-126, 2018.

449 Blake, Jr., W.: Holocene emergence along the Ellesmere Island coast of northernmost Baffin Bay,  
450 Norsk Geologisk Tidsskrift, 73, 147-160, 1993.

451 Borchers, B., Marrero, S., Balco, G., Caffee, M., Goehring, B., Lifton, N., Nishiizumi, K., Phillips, F.,  
452 Schaefer, J., Stone, J.: Geological calibration of spallation production rates in the CRONUS Earth  
453 project, Quaternary Geochronology, 31, 188-198, 2016.

454 Bradwell, T., Fabel, D., Clark, C. D., Chiverrell, R. C., Small, D., Smedley, R. K., Saher, M. H., Moreton,  
455 S. G., Dove, D., Callard, S. L., Duller, G. A. T., Medialdea, A., Bateman, M. D., Burke, M. J., McDonald,  
456 N., Gilgannon, S., Morgan, S., Roberts, D. H., Ó Cofaigh, C.: Pattern, style and timing of British-Irish Ice  
457 Sheet advance and retreat over the last 45 000 years: evidence from NW Scotland and the adjacent  
458 continental shelf, Journal of Quaternary Science, 36, 871-933, 2021.

459 Briner, J. P., Gosse, J. C., Bierman, P. R.: Applications of cosmogenic nuclides to Laurentide Ice Sheet  
460 history and dynamics, Geological Society of America, Special Paper, 415, 29-41, 2006.

461 Briner, J. P., Lifton, N. A., Miller, G. H., Refsnider, K., Anderson, R. K., Finkel, R.: Using *in situ*  
462 cosmogenic  $^{10}\text{Be}$ ,  $^{14}\text{C}$ , and  $^{26}\text{Al}$  to decipher the history of polythermal ice sheets, Quaternary  
463 Geochronology, 19, 4-13, 2014.

465 Brunnberg, L.: Clay-varve Chronology and Deglaciation during the Younger Dryas and Preboreal in the  
466 Easternmost Part of the Middle Swedish Ice Marginal Zone, Department of Quaternary Research,  
467 Quaternaria A2, Stockholm University, Stockholm, 1-94, 1995.

468 Dalton, A.S., Dulfer, H.E., Margold, M., Heyman, J., Clague, J.J., Froese, D.G., Gauthier, M.S., Hughes,  
469 A.L.C., Jennings, C.E., Norris, S.L., Stoker, B.J.: Deglaciation of the north American ice sheet complex

470 in calendar years based on a comprehensive database of chronological data: NADI-1, Quaternary  
471 Science Reviews, 321, 108345, 2023.

472 Dalton, A. S., Margold, M., Stokes, C. R., Tarasov, L., Dyke, A. S., Adams, R. S., Allard, S., Arends, H. E.,  
473 Atkinson, N., Attig, J. W., Barnett, P. J., Barnett, R. L., Batterson, M., Bernatchez, P., Borns Jr., H. W.,  
474 Breckenridge, A., Briner, J. P., Brouard, E., Campbell, J. E., Carlson, A. E., Clague, J. J., Curry, B. B.,  
475 Daigneault, R. A., Dubé-Loubert, H., Easterbrook, D. J., Franzi, D. A., Friedrich, H. G., Funder, S.,  
476 Gauthier, M. S., Gowan, A. S., Harris, K. L., Hétu, B., Hooyer, T. S., Jennings, C. E., Johnson, M. D.,  
477 Kehew, A. E., Kelley, S. E., Kerr, D., King, E. L., Kjeldsen, K. K., Knaeble, A. R., Lajeunesse, P., Lakeman,  
478 T. R., Lamothe, M., Larson, P., Lavoie, M., Loope, H. M., Lowell, T. V., Lusardi, B. A., Manz, L.,  
479 McMartin, I., Nixon, F. C., Occhietti, S., Parkhill, M. A., Piper, D. J. W., Pronk, A. G., Richard, P. J. H.,  
480 Ridge, J. C., Ross, M., Roy, M., Seaman, A., Shaw, J., Stea, R. R., Teller, J. T., Thompson, W. B.,  
481 Thorleifson, L. H., Utting, D. J., Veillette, J. J., Ward, B. C., Weddle, T. K., Wright, H. E.: An updated  
482 radiocarbon-based ice margin chronology for the last deglaciation of the North American Ice Sheet  
483 Complex, Quaternary Science Reviews, 234, 106223, 2020.

484 De Geer, G.: The transbaltic extension of the Swedish Time Scale, Geografiska Annaler, 17, 533-549,  
485 1935.

486 De Geer, G.: Geochronologia Suecica principes, Kungliga svenska vetenskapsakademien Handlingar,  
487 III, Bd 18, 6, 1–367, 1940.

488 Dyke, A. S., Morris, T. F., Green, D. E. C., England, J.: Quaternary geology of Prince of Wales Island,  
489 Arctic Canada, Geological Survey of Canada, Memoir, 433, 1–142, 1992.

490 Dyke, A. S., Andrews, J. T., Clark, P. U., England, J. H., Miller, G. H., Shaw, J., Veillette, J. J.: The  
491 Laurentide and Innuitian ice sheets during the Last Glacial Maximum, Quaternary Science Reviews,  
492 21, 9–31, 2002.

493 Fogwill, C., Turney, C., Gollidge, N., Rood, D., Hippe, K., Wacker, L., Jones, R.: Drivers of abrupt  
494 Holocene shifts in West Antarctic ice stream direction determined from combined ice sheet  
495 modelling and geologic signatures. Antarctic Science, 26, 674–686, 2014.

496 Goehring, B. M., Schaefer, J. M., Schluechter, C., Lifton, N. A., Finkel, R. C., Jull, A. J. T., Akçar, N.,  
497 Alley, R. B.: The Rhone Glacier was smaller than today for most of the Holocene, Geology, 39, 679–  
498 682, 2011.

499 Gosse, J. C., Phillips, F. M.: Terrestrial *in situ* cosmogenic nuclides: theory and application, Quaternary  
500 Science Reviews, 20, 1475–1560, 2001.

501 Greenwood, S. L., Simkins, L. M., Winsborrow, M. C. M., Bjarnadóttir, L. R.: Exceptions to bed-  
502 controlled ice sheet flow and retreat from glaciated continental margins worldwide, Science  
503 Advances, 7, eabb6291, 2021.

504 Greenwood, S. L., Clason, C. C., Nyberg, J., Jakobsson, M., Holmlund, P.: The Bothnian Sea ice stream:  
505 early Holocene retreat dynamics of the south-central Fennoscandian Ice Sheet, Boreas, 46, 346-362,  
506 2017.

507 Hall A. M., Ebert K., Goodfellow B. W., Hättestrand C., Heyman J., Krabbendam M., Moon S., Stroeven  
508 A. P.: Past and future impact of glacial erosion in Forsmark and Uppland. TR-19-07 Svensk  
509 Kärnbränslehantering AB, 2019.

510 Hall, A. M., Krabbendam, M., van Boeckel, M., Goodfellow, B. W., Hättestrand, C., Heyman, J.,  
511 Palamakumbura, R. N., Stroeven A. P., Näslund, J.-O.: Glacial ripping: geomorphological evidence  
512 from Sweden for a new process of glacial erosion, *Geografiska Annaler*, 102, 333-353, 2020.

513 Hedenström, A., Risberg, J.: Shore displacement in northern Uppland during the last 6500 calendar  
514 years, TR-03-17 Svensk Kärnbränslehantering AB, 2003.

515 Heyman, J., Stroeven, A. P., Harbor, J. M., Caffee, M. W.: Too young or too old: Evaluating  
516 cosmogenic exposure dating based on an analysis of compiled boulder exposure ages, *Earth and  
517 Planetary Science Letters*, 302, 71–80, 2011.

518 Hippe, K., Lifton, N. A.: Calculating isotope ratios and nuclide concentrations for *in situ* cosmogenic  
519 <sup>14</sup>C Analyses, *Radiocarbon*, 56, 1167–1174, 2014.

520 Hippe, K., Ivy-Ochs, S., Kober, F., Zasadni, J., Wieler, R., Wacker, L., Kubik, P.W., Schlüchter, C.:  
521 Chronology of Lateglacial ice flow reorganization and deglaciation in the Gotthard Pass area, Central  
522 Swiss Alps, based on cosmogenic <sup>10</sup>Be and *in situ* <sup>14</sup>C, *Quaternary Geochronology*, 19, 14–26, 2014.

523 Hughes, A. L. C., Gyllencreutz, R., Lohne, Ø. S., Mangerud, J., Svendsen, J. I.: The last Eurasian ice  
524 sheets – a chronological database and time-slice reconstruction, *DATED-1, Boreas*, 45, 1–45, 2016.

525 Ivy-Ochs, S., Kober, F.: Surface exposure dating with cosmogenic nuclides, *Quaternary Science  
526 Journal*, 57, 157–189, 2008.

527 Kleman, J., Hättestrand, M., Borgström, I., Preusser, F., Fabel, D.: The Idre marginal moraine—an  
528 anchorpoint for Middle and Late Weichselian ice sheet chronology, *Quaternary Science Advances*, 2,  
529 100010, 2020.

530 Kleman, J., Stroeven, A. P., Lundqvist, J.: Patterns of Quaternary ice sheet erosion and deposition in  
531 Fennoscandia and a theoretical framework for explanation, *Geomorphology*, 97, 73–90, 2008.

532 Koester, A., Lifton, N. A.: Technical note: A software framework for calculating compositionally  
533 dependent *in situ* <sup>14</sup>C production rates, *Geochronology*, 5, 21–33, 2023.

534 Lal, D.: Cosmic ray labeling of erosion surfaces: *in situ* nuclide production rates and erosion rates,  
535 *Earth and Planetary Science Letters*, 104, 424–439, 1991.

536 Lambeck, K., Purcell, A., Zhao, J., Svensson, N.-O.: The Scandinavian Ice Sheet: from MIS 4 to the end  
537 of the Last Glacial Maximum, *Boreas*, 39, 410-435, 2010.

538 Lambeck, K., Smither, C., Johnston, P.: Sea-level change, glacial rebound and mantle viscosity for  
539 northern Europe, *Geophysical Journal International*, 134, 102-134, 1998.

540 Lidberg, M., Johansson, J. M., Scherneck, H.-G., Milne, G. A.: Recent results based on continuous GPS  
541 observations of the GIA process in Fennoscandia from BIFROST, *Journal of Geodynamics*, 50, 8–18,  
542 2010.

543 Lifton, N.: Implications of two Holocene time-dependent geomagnetic models for cosmogenic nuclide  
544 production rate scaling, *Earth and Planetary Science Letters*, 433, 257–268, 2016.

545 Lifton, N., Caffee, M., Finkel, R., Marrero, S., Nishiizumi, K., Phillips, F. M., Goehring, B., Gosse, J.,  
546 Stone, J., Schaefer, J., Theriault, B.: *In situ* cosmogenic nuclide production rate calibration for the  
547 CRONUS-Earth project from Lake Bonneville, Utah, shoreline features, *Quaternary Geochronology*,  
548 26, 56–69, 2015.

549 Lifton, N., Sato, T., and Dunai, T. J.: Scaling *in situ* cosmogenic nuclide production rates using  
550 analytical approximations to atmospheric cosmic-ray fluxes, *Earth and Planetary Science Letters*, 386,  
551 149–160, 2014.

552 Lifton, N., Wilson, J., Koester, A.: Technical note: Studying Li-metaborate fluxes and extraction  
553 protocols with a new, fully automated *in situ* cosmogenic  $^{14}\text{C}$  processing system at PRIME Lab,  
554 *Geochronology*, 5, 361–375, 2023.

555 Long, A. J., Woodroffe, S. A., Roberts, D. H., Dawson, S.: Isolation basins, sea-level changes and the  
556 Holocene history of the Greenland Ice Sheet, *Quaternary Science Reviews*, 30, 3748–3768, 2011.

557 Lönnqvist, M., Hökmark, H.: Approach to estimating the maximum depth for glacially induced  
558 hydraulic jacking in fractured crystalline rock at Forsmark, Sweden, *Journal of Geophysical Research:*  
559 *Earth Surface*, 118, 1777–1791, 2013.

560 Lupker, M., Hippe, K., Wacker, L., Kober, F., Maden, C., Braucher, R., Bourlès, D., Romani, J. R. V.,  
561 Wieler, R.: Depth-dependence of the production rate of *in situ*  $^{14}\text{C}$  in quartz from the Leymon High  
562 core, Spain, *Quaternary Geochronology*, 28, 80–87, 2015.

563 Margold, M., Gosse, J. C., Hidy, A. J., Woywitka, R. J., Young, J. M., Froese, D.: Beryllium-10 dating of  
564 the Foothills Erratics Train in Alberta, Canada, indicates detachment of the Laurentide Ice Sheet from  
565 the Rocky Mountains at ~15 ka, *Quaternary Research*, 92, 469–482, 2019.

566 Marrero, S. M., Phillips, F. M., Caffee, M. W., Gosse, J. C.: CRONUS-Earth cosmogenic  $^{36}\text{Cl}$  calibration,  
567 *Quaternary Geochronology*, 31, 199–219, 2016.

568 Matmon, A., Crouvi, O., Enzel, Y., Bierman, P., Larsen, J., Porat, N., Amit, R., Caffee, M.: Complex  
569 exposure histories of chert clasts in the late Pleistocene shorelines of Lake Lisan, southern Israel.  
570 *Earth Surface Processes and Landforms* 28, 493–506, 2003.

571 Miller, G. H., Briner, J. P., Lifton, N. A., Finkel, R. C.: Limited ice-sheet erosion and complex exposure  
572 histories derived from *in situ* cosmogenic  $^{10}\text{Be}$ ,  $^{26}\text{Al}$ ,  $^{14}\text{C}$  on Baffin Island, Arctic Canada, *Quaternary*  
573 *Geochronology*, 1, 74–85, 2006.

574 Moon, S., Perron, J. T., Martel, S.J., Goodfellow, B.W., Mas Ivars, D., Hall, A., Heyman, J., Munier, R.,  
575 Näslund, J.-O., Simeonov, A., Stroeven, A.P.: Present-day stress field influences bedrock fracture  
576 openness deep into the subsurface. *Geophysical Research Letters* 47, e2020GL090581, 2020.

577 Norris, S. L., Tarasov, L., Monteath, A. J., Gosse, J. C., Hidy, A. J., Margold, M., Froese, D. G.: Rapid  
578 retreat of the southwestern Laurentide Ice Sheet during the Bølling-Allerød interval, *Geology*, 50,  
579 417–421, 2022.

580 Pässe, T., Andersson, L: Shore-level displacement in Fennoscandia calculated from empirical data,  
581 *GFF*, 127, 253–268, 2005.

582 Patton, H., Hubbard, A., Andreassen, K., Auriac, A., Whitehouse, P. L., Stroeven, A. P., Shackleton, C.,  
583 Winsborrow, M., Heyman, J., Hall, A. M.: Deglaciation of the Eurasian ice sheet complex, *Quaternary*  
584 *Science Reviews*, 169, 148–172, 2017.

585 Patton, H., Hubbard, A., Andreassen, K., Winsborrow, M., Stroeven, A.P.: The build-up, configuration,  
586 and dynamical sensitivity of the Eurasian ice-sheet complex to Late Weichselian climatic and oceanic  
587 forcing, *Quaternary Science Reviews*, 153, 97–121, 2016.

588 Patton, H., Hubbard, A., Heyman, J., Alexandropoulou, N., Lasabuda, A. P. E., Stroeven, A.P., Hall,  
589 A.M., Winsborrow, M., Sugden, D.E., Kleman, J., Andreassen, K.: The extreme yet transient nature of  
590 glacial erosion, *Nature Communications* 13, 7377, 2022.

591 Pendleton, S., Miller, G., Lifton, N., Young, N.: Cryosphere response resolves conflicting evidence for  
592 the timing of peak Holocene warmth on Baffin Island, Arctic Canada, *Quaternary Science*  
593 *Reviews*, 216, 107–115, 2019.

594 Phillips, F. M., Argento, D. C., Balco, G., Caffee, M. W., Clem, J., Dunai, T. J., Finkel, R., Goehring, B.,  
595 Gosse, J. C., Hudson, A. M., Jull, A. J. T., Kelly, M. A., Kurz, M., Lal, D., Lifton, N., Marrero, S. M.,  
596 Nishiizumi, K., Reedy, R. C., Schaefer, J., Stone, J. O. H., Swanson, T., Zreda, M. G.: The CRONUS-Earth  
597 Project: A synthesis, *Quaternary Geochronology*, 31, 119–154, 2016.

598 Rainio, H., Kejonen, A., Kielosto, S., Lahermo, P.: Avancerade inlandsisen på nytt också till  
599 Mellanfinska randformationen? *Geologi*, 38, 95–109, 1986.

600 Regnéll, C., Becher, G. P., Öhrling, C., Greenwood, S. L., Gyllencreutz, R., Blomdin, R., Brendryen, J.,  
601 Goodfellow, B. W., Mikko, H., Ransed, G., Smith, C.: Ice-dammed lakes and deglaciation history of the  
602 Scandinavian Ice Sheet in central Jämtland, Sweden, *Quaternary Science Reviews*, 314, 108219, 2023.

603 Risberg, J.: Strandförskjutningen i nordvästra Uppland under subboreal tid. In Segerberg, A. Bälunge  
604 mossar: kustbor i Uppland under yngre stenålder, PhD Thesis. Uppsala University, Appendix 4. (in  
605 Swedish), 1999.

606 Robertsson, A.-M., Persson, C.: Biostratigraphical studies of three mires in northern Uppland,  
607 Sweden, *Sveriges geologiska undersökning*, (Serie C 821.), 1989.

608 Romundset, A., Bondevik, S., Bennike, O.: Postglacial uplift and relative sea level changes in  
609 Finnmark, northern Norway, *Quaternary Science Reviews*, 30, 2398–2421, 2011.

610 Schildgen, T. F., Phillips, W. M., Purves, R. S.: Simulation of snow shielding corrections for cosmogenic  
611 nuclide surface exposure studies, *Geomorphology*, 64, 67–85, 2005.

612 Schimmelpfennig, I., Schaefer, J. M., Goehring, B. M., Lifton, N., Putnam, A. E., Barrell, D. J.:  
613 Calibration of the *in situ* cosmogenic <sup>14</sup>C production rate in New Zealand's Southern Alps, *Journal of*  
614 *Quaternary Science*, 27, 671–674, 2012.

615 Schimmelpfennig, I., Schaefer, J. M., Lamp, J., Godard, V., Schwartz, R., Bard, E., Tuna, T., Akçar, N.,  
616 Schlüchter, C., Zimmerman, S., and ASTER Team: Glacier response to Holocene warmth inferred from  
617 *in situ* <sup>10</sup>Be and <sup>14</sup>C bedrock analyses in Steingletscher's forefield (central Swiss Alps), *Climate of the*  
618 *Past*, 18, 23–44, 2022.

619 Schweinsberg, A. D., Briner, J. P., Miller, G. H., Lifton, N. A., Bennike, O., & Graham, B. L.: Holocene  
620 mountain glacier history in the Sukkertoppen Iskappe area, southwest Greenland, *Quaternary*  
621 *Science Reviews*, 197, 142–161, 2018.

622 SGU: Högsta Kustlinjen (in Swedish) [https://resource.sgu.se/dokument/produkter/hogsta-kustlinjen-](https://resource.sgu.se/dokument/produkter/hogsta-kustlinjen-beskrivning)  
623 [beskrivning](https://resource.sgu.se/dokument/produkter/hogsta-kustlinjen-beskrivning) (Geological Survey of Sweden), 2015.

624 Simkins, L. M., Simms, A. R., DeWitt, R.: Relative sea-level history of Marguerite Bay, Antarctic  
625 Peninsula derived from optically stimulated luminescence-dated beach cobbles, *Quaternary Science*  
626 *Reviews*, 77, 141–155, 2013.

627 SKB: Post-closure safety for the final repository for spent nuclear fuel at Forsmark – Climate and  
628 climate-related issues, PSAR version, TR-20-12, Svensk Kärnbränslehantering AB, 2020.

629 SKB: Post-closure safety for the final repository for spent nuclear fuel at Forsmark – Main report,  
630 PSAR version. SKB TR-21-01, Svensk Kärnbränslehantering AB, 2022.

631 Steffen, H., Wu, P.: Glacial isostatic adjustment in Fennoscandia - A review of data and modeling,  
632 *Journal of Geodynamics*, 52, 169–204, 2011.

633 Steinemann, O., Ivy-Ochs, S., Hippe, K., Christl, M., Haghypour, N., and Synal, H. A.: Glacial erosion by  
634 the Trift glacier (Switzerland): Deciphering the development of riegels, rock basins and gorges,  
635 *Geomorphology*, 375, 107533, 2021.

636 Stephens, M. B., Jansson, N. F.: Chapter 6, Paleoproterozoic (1.9–1.8 Ga) syn-orogenic magmatism,  
637 sedimentation and mineralization in the Bergslagen lithotectonic unit, Svecokarelian orogen. In M B  
638 Stephens & J Bergman Weihed (eds.): Sweden: Lithotectonic Framework, Tectonic Evolution and  
639 Mineral Resources, Geological Society of London Memoirs, 50, 105–206, 2020.

640 Stroeven, A. P., Hättstrand, C., Kleman, J., Heyman, J., Fabel, D., Fredin, O., Goodfellow, B. W.,  
641 Harbor, J. M., Jansen, J. D., Olsen, L., Caffee, M. W., Fink, D., Lundqvist, J., Rosqvist, G. C., Strömberg,  
642 B., Jansson, K. N.: Deglaciation of Fennoscandia, *Quaternary Science Reviews*, 147, 91–12, 2016.

643 Stroeven, A.P., Heyman, J., Fabel, D., Björck, S., Caffee, M.W., Fredin, O., Harbor, J.M.: A new  
644 Scandinavian reference <sup>10</sup>Be production rate, *Quaternary Geochronology*, 29, 104–115, 2015.

645 Strömberg, B.: Late Weichselian deglaciation and clay varve chronology in east-central Sweden,  
646 *Sveriges geologiska undersökning (Ser. Ca 73)*, 1989.

647 Strömberg, B.: Younger Dryas deglaciation at Mt. Billingen, and clay varve dating of the Younger  
648 Dryas/Preboreal transition, *Boreas*, 23, 177-193, 1994.

649 Wohlfarth, B., Björck, S., Possnert, G.: The Swedish Time Scale: a potential calibration tool for the  
650 radiocarbon time scale during the late Weichselian, *Radiocarbon*, 37, 347-359, 1995.

651 Young, N. E., Lesnek, A. J., Cuzzone, J. K., Briner, J. P., Badgeley, J. A., Balter-Kennedy, A., Graham, B.  
652 L., Cluett, A., Lamp, J. L., Schwartz, R., Tuna, T., Bard, E., Caffee, M. W., Zimmerman, S. R. H.,  
653 Schaefer, J. M.: *In situ* cosmogenic <sup>10</sup>Be–<sup>14</sup>C–<sup>26</sup>Al measurements from recently deglaciated bedrock as  
654 a new tool to decipher changes in Greenland Ice Sheet size, *Climate of the Past*, 17, 419–450, 2021.

655 Young, N. E., Schaefer, J. M., Goehring, B., Lifton, N., Schimmelpfennig, I., Briner, J. P.: West  
656 Greenland and global *in situ* <sup>14</sup>C production-rate calibrations, *Journal of Quaternary Science*, 29, 401–  
657 406, 2014.